Korean J. Chem. Eng., 39(11), 3012-3020 (2022)
DOI: 10.1007/s11814-022-1238-5

pISSN: 0256-1115
eISSN: 1975-7220

Numerical investigation of factors affecting carbon deposition and interaction on SOFC performance over time

Hamed Khoshkam*, Kazem Atashkari*,†, and Mehdi Borji**

*Department of Mechanical Engineering, the University of Guilan, P. O. Box 3756, Rasht, Iran
**Department of Mechanical Engineering, Lahijan Branch, Islamic Azad University, Lahijan, Iran
(*Received 1 February 2022 • Revised 29 June 2022 • Accepted 19 July 2022*)

Abstract−One of the weaknesses of the fuel cell is the phenomenon of carbon deposition when using hydrocarbon fuel. Investigating the factors affecting the amount of carbon deposition can improve the performance of the fuel cell, efficiency and life time. A time-dependent two-dimensional numerical model based on the finite element method that considers the carbon deposition has been developed to evaluate the effect of velocity, temperature and hydrogen mole fraction as fuel constituent on the carbon deposition rate and porosity variations. The results were found in good agreement with the available published experimental and numerical data in terms of cell operating voltage, power density and carbon deposition rate. The carbon deposition rate accelerates with increasing operating temperature, inlet molar fraction of hydrogen, and decreasing the inlet velocity. Carbon deposition reduces porosity and catalyst activity. Due to the above mentioned variations, the electric power generated by the fuel cell is drastically reduced, leading to reduced electric efficiency.

Keywords: Solid Oxide Fuel Cell (SOFC), Carbon Deposition, Porosity Change, Numerical Simulation, Parameter Analysis

INTRODUCTION

High efficiency, specific gravimetric and volumetric energy density, potentially low greenhouse gas emissions and more flexibility in the use of hydrocarbon fuels have increased the attention to solid oxide fuel cells. A fuel cell consumes a wide range of fuels, from pure hydrogen to hydrocarbons such as natural gas and biogas [1,2]. Fuel cell performance and efficiency are affected by several parameters, including temperature, inlet velocity of gases, working pressure, inlet fuel composition, material, cell geometry, and flow direction [3]. Improving the efficiency and the useful lifetime of solid oxide fuel cells (SOFCs) is very important; therefore, optimization factors have received considerable attention [4-6]. CHP systems are an attractive fuel cell application that increases the maximum utilization of chemical fuel energy [7-9]. In the hydrocarbon-fed SOFC, carbon deposition on the surface of catalyst Ni is undeniable [10]. Carbon deposition reduces the anode porosity and catalyst activity, and attenuates the diffusion coefficients, the charge conductivity and the thermal conductivity [11]. A thermodynamic solution is a way to determine the boundary of carbon formation. Temperature, type of solid electrolyte, and the extent of the electrochemical reaction of hydrogen are the key parameters of carbon formation [12]. In the thermodynamic analysis some assumptions cannot be justified: the rates of the forward reaction (carbon deposition) and the reverse reaction (carbon removal) are rapid enough to establish equilibrium [13]. The effect of increasing temperature on the amount of carbon deposition increment and performance of the fuel cell highlights the importance of operating temperature [14]. Subotic et al. [15] showed that a higher methane concentration will lead to faster carbon formation. If the concentration of carbon monoxide is noticeably higher than methane concentration, it will be possible to produce carbon on the anode side of the cell. The impact on the carbon formation increases from carbon dioxide through carbon monoxide to methane, while the methane concentration has a decisive influence on the carbon formation, and the results indicate that humidity significantly reduces the carbon formation rate. Kim et al. [16] indicated how carbon deposition fills the pores and deactivates the anode; also they showed that if the surface of the anodes contains catalytically active compounds, such as ceria, it will be possible that steam generated in the electrochemical reactions be used to avoid carbon formation. Yang et al. [17] used a physical thermodynamic-mathematical model to study carbon deposition and methane conversion rate. They found that under an operating temperature of 800 °C and porosity of ε=0.4, the methane conversion rate can reach its maximum value. The results also showed that the smaller Ni particle in porous support layer will be followed by the easier carbon deposition on catalyst surface. Han Xu et al. [18] used the lattice Boltzmann model (LB) to show the distribution of carbon deposition. They showed the effect of heterogeneity of anode microstructure on carbon deposition, and also decreasing the operating temperature and increasing the pre-reforming extent of methane on the suppression of carbon deposition. He et al. [19] showed that the higher the temperature, the stronger the carbon bond, therefore making it more difficult to clean the surface from carbon. At 600 °C to 1,000 °C, carbon is formed as graphite. Below 600 °C, it is seen as a carbon nanofibers that do not exist at high temperatures [20]. Research has shown that under certain conditions, precipitated carbon can be easily removed from the electrolyte surface. But in

†To whom correspondence should be addressed.
E-mail: atashkar@guilan.ac.ir

some cases it is very difficult and somewhat impossible to remove the deposited carbon [21,22]. Schluckner et al. [23] proposed a new thermodynamic approach for estimating carbon deposition. They examined the deposition of two types of carbon in a porous medium to investigate different conditions and different ratios of fuels and components. They found that variations in micro-structures near the anode surface are factors in the destruction of the fuel cell in carbon deposition. SOFC has been investigated numerically by use of different mathematical models, considering electrochemical model, momentum, energy and specious mass conservation equations [24-26].

In the present study, a complete numerical method was used in seven separate sections, namely, the air and fuel flow channels, the cathode and anode support and catalyst layers, and the electrolyte. The time dependent governing equations with suitable boundary conditions were solved by use of COMSOL Multiphysics commercial software. All the important electrochemical and chemical reactions, such as methane cracking reaction (MCR), water-gas shift reaction (WGSR), Boudouard reaction (BR), methane steam reforming reaction (MSRR) and CO, and H_2 oxidation, were solved in a specified layer simultaneously affected by other layers. Time dependent carbon deposition and its effect on the anode porosity and thereby cell electric performance under different operating conditions, such as fuel inlet velocity and hydrogen mole fraction as well as operating temperature, were numerically analyzed.

PHYSICAL MODELS AND REACTIONS

Fig. 1 shows the anode-supported solid oxide fuel cell schematic diagram, including air and fuel channels, cathode support layer, anode support layer, cathode reaction layer, anode reaction layer and electrolyte. Four main reactions, WGSR, MCR, MSRR, and BR, occur inside the anode support layer. Electrochemical reactions of carbon monoxide and hydrogen occur in the reaction zone in the presence of oxygen ions passing through the electrolyte.

Syngas fuel, which is composed of CH_4, CO, H_2, CO_2, and H_2O, flows thorough the fuel channel and air, mainly consisting of N_2 and O_2 entering the air channel. The composition of fuel enters the anode channel and other SOFC main geometrical and operating conditions are given in Table 1.

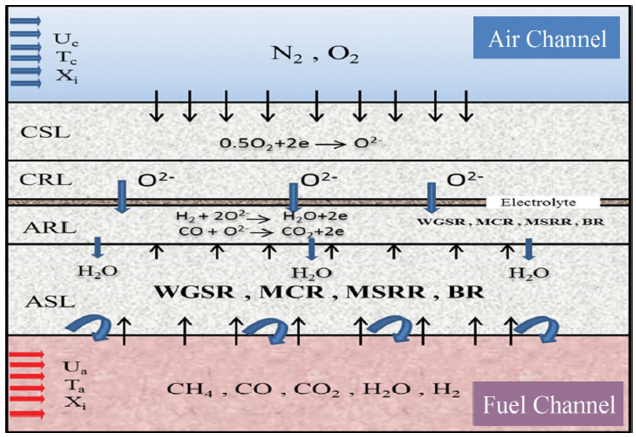

Fig. 1. Schematic of planar SOFC.

As mentioned above, methane, hydrogen, carbon dioxide, carbon monoxide and water vapor are considered as the input fuel components. Four dominant chemical reactions and two electrochemical reactions considered in the present model are as follows:

$CH_4 \Leftrightarrow C+2H_2$ (MSRR)

$CO+H_2 \Leftrightarrow C+H_2O$ (BR)

$CO+H_2O \Leftrightarrow CO_2+H_2O$ (WGSR)

$CH_4 \Leftrightarrow C+2H_2$ (MCR)

$H_2+\frac{1}{2}O_2 \rightarrow H_2O$ $\quad CO+\frac{1}{2}O_2 \rightarrow CO_2$ Electrochemical reactions

$H_2+O^{2-} \rightarrow H_2O+2e^-$ Anode

$CO+O^{2-} \rightarrow CO_2+2e^-$ Anode

$\frac{1}{2}O_2+2e^- \rightarrow O^{2-}$ cathode

1. Electrochemical Model

The three-phase boundary (TPB) is the most active place where most electrochemical reactions take place. This part is located at a distance of 10 μm from the electrolyte [29]. The relation between activation polarization and electric current intensity was calculated

Table 1. Physical dimension and working parameters of the model [24,27]

Working temperature	1,000-1,123 K	Inlet molar fraction of N_2	% 0.79
Length of the cell	0.1 m	Inlet molar fraction of O_2	% 0.21
Initial porosity of anode	0.4	Inlet molar fraction of H_2	% 0.044
Porosity of cathode	0.4	Inlet molar fraction of CO	% 0.493
Working pressure	1 atm	Inlet molar fraction of CO_2	% 0.029
Height of fuel channel	1×10^{-3} m	Inlet molar fraction of CH_4	% 0.263
Height of air channel	1×10^{-3} m	Inlet molar fraction of H_2O	% 0.171
Cathode supported layer thickness	2.5×10^{-5} m	Aperture of cathode supported layer	1.4×10^{-6} m
Anode supported layer thickness	4×10^{-4} m	Aperture of anode supported layer	2×10^{-6} m
Thickness of electrolyte	8×10^{-6} m	Tortuosity of electrode	4.5
Cathode reaction layer thickness	1.3×10^{-3} m	Faraday's constant	96,487
Anode reaction layer thickness	2×10^{-3} m	Inlet velocity	1, 2, 3 m s^{-1}

by the well-known Butler-Volmer equation [6]:

$$j = j_0\left\{\exp\left(\frac{\alpha\eta_{act,\,i}n_eF}{RT}\right) - \exp\left(\frac{-(1-\alpha)\eta_{act,\,i}n_eF}{RT}\right)\right\} \quad (1)$$

The rates of each reaction are as follows:

$$\dot{r}_{elec,\,H_2} = \dot{r}_{elec,\,H_2O} = \frac{j_{H_2}}{2F} \quad (2)$$

$$\dot{r}_{elc,\,CO} = \dot{r}_{elec,\,CO_2} = \frac{j_{CO}}{2F} \quad (3)$$

$$\dot{r}_{elec,\,O_2} = \frac{j_{O_2}}{4F} \quad (4)$$

Considering H_2 and CO electrochemical reactions, the cell open circuit potential can be calculated based on Nernst equation as follows [30,31]:

$$E^{rev}_{H_2-O_2} = E^0_{H_2-O_2} - \frac{R_uT}{2F}\ln\left[\frac{P^{fc}_{H_2O}}{P^{fc}_{H_2}\cdot\left(\frac{P^{ac}_{O_2}}{100{,}000}\right)^{0.5}}\right] \quad (5)$$

$$E^{rev}_{CO-O_2} = E^0_{CO-O_2} - \frac{R_uT}{2F}\ln\left[\frac{P^{fc}_{CO_2}}{P^{fc}_{CO}\cdot\left(\frac{P^{ac}_{O_2}}{100{,}000}\right)^{0.5}}\right] \quad (6)$$

If an electrical current is drawn from a fuel cell, the voltage reduces in response to five loss mechanisms of a cell: electrode activation and concentration over potentials and internal resistances, So cell operating potential can be calculated by use of the following correlation:

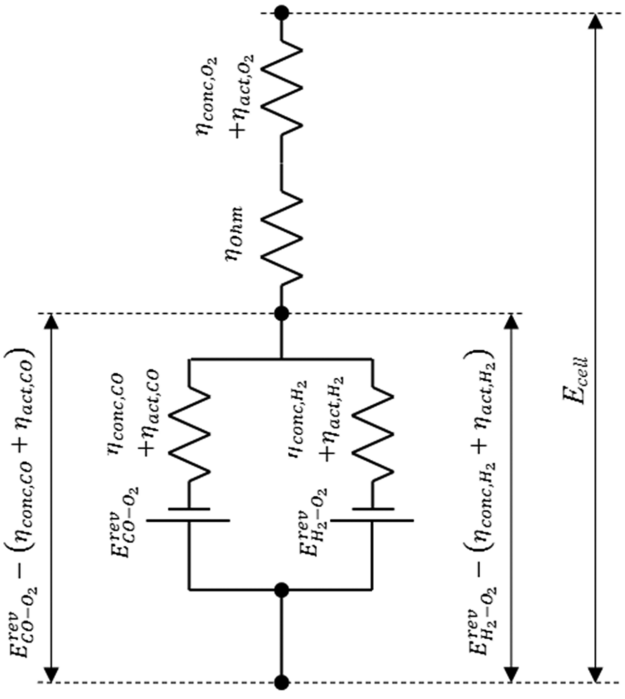

Fig. 2. Equivalent circuit model for current and voltage calculations.

$$E_{cell} = E^{rev}_{H_2-O_2} - (\eta_{conc,\,O_2} + \eta_{act,\,O_2}) - (\eta_{conc,\,H_2} + \eta_{act,\,H_2}) - \eta_{Ohm} \quad (7)$$

$$E_{cell} = E^{rev}_{CO-O_2} - (\eta_{conc,\,O_2} + \eta_{act,\,O_2}) - (\eta_{conc,\,CO} + \eta_{act,\,CO}) - \eta_{Ohm} \quad (8)$$

According to the iterative procedure proposed by Iwai et al. [34], the ratio of j_{H_2} and j_{CO} is determined so that the potentials obtained for parallel parts of Fig. 2 to match each other.

The conservation of electronic and ionic charge in the interconnect layer is as follows:

$\nabla\cdot j_l = 0$ conservation of ionic charge
$\nabla\cdot j_s = 0$ conservation of electronic charge

where (j) is the current density, and it is described by Ohm's law as follows:

$$j_l = -\sigma_l\nabla\varphi_{el} \quad (9)$$

$$j_s = -\sigma_s\nabla\varphi_{i0} \quad (10)$$

where σ is the electronic or ionic conductivity and $\nabla\varphi$ is the electronic or ionic potential.

2. Momentum Conservation

The velocity of the fluid flow in the cathodic and anodic channels along with porous electrodes affects the rate of heat transfer in the cell and plays an important role in controlling the cell operating temperature. Furthermore, the effect of chemical reaction rates influenced by temperature field on the electric performance of the cell cannot be ignored. Despite the fact that at high electric currents or low voltages, the models considering momentum equation give more accurate results [32], many researches do not take it into account.

In this study, the well-known Navier-stokes equation was used to calculate the variation of velocity and pressure inside the flow [27]:

$$\frac{\partial\rho}{\partial t} + \nabla\cdot(\rho u) = S \quad (11)$$

$$\rho\frac{\partial u}{\partial t} - \nabla\cdot[\eta(\nabla u + (\nabla u)^T)] + \rho(u\cdot\nabla)u + \nabla p = S \quad (12)$$

Brinkman equation is employed in porous electrode support and reaction layers [27]:

$$\frac{\partial\varepsilon\rho}{\partial t} + \nabla\cdot(\rho u) = S \quad (13)$$

$$\frac{\rho\partial u}{\varepsilon\partial t} + \left(\frac{\eta}{k} + S\right)u = \nabla\cdot\left[\frac{\eta}{\varepsilon}(\nabla u + (\nabla u)^T)\right] - \nabla p \quad (14)$$

In this equation μ stands for the dynamic viscosity and S introduces the momentum source terms for each calculation domain: anode support and reaction layer (ASL, and ARL), cathode reaction layer (CRL) and fuel flow channel, which are listed below [27].

S_{ASL} $R-msrr(MCO+3M_{H2}-MCH_4-MH_2O)$
$+R-wgsr(MCO_2+MH_2-MCO-MH_2O)$
$+R-mcr(2MH_2-MCH_4)+R-BR(MCO_2-2MCO)$

S_{fuel} $R-wgsr(MCO_2+MH_2-MCO-MH_2O)$

S_{CRL} $\frac{-JM_{O_2}}{4F}$

$$S_{ARL}\ \ R-msrr(MCO+3MH_2-MCH_4-MH_2O)+R-wgsr(MCO_2+MH_2-MCO-MH_2O)+R-mcr(2MH_2-MCH_4)+R-BR(MCO_2-2MCO)+\frac{J(M_{H_2O}-M_{H_2})}{2F}+\frac{J(M_{CO_2}-M_{CO})}{2F}$$

The parameters R_{msrr}, R_{wgsr}, R_{mcr}, and R_{BR} are the rate of MSRR, WGSR, MCR, and BR, respectively. These parameters can be defined mathematically as follows [27]:

$$R_{msrr}=a(K_{f,msr}P_{CH_4}P_{H_2O}-K_{b,msr}P_{CO}P_{H_2}) \quad (15)$$

$$R_{wgsr}=a(K_{f,wgsr}P_{CO}P_{H_2O}-K_{b,wgsr}P_{CO_2}P_{H_2}) \quad (16)$$

$$R_{mcr}=a\left(\frac{1}{3600M_c}\frac{K_{f,mcr}(P_{CH_4}-P_{H_2}^2/K_{p,mcr})}{(1+K_{H_2}\sqrt{P_{H_2}})^2}\right) \quad (17)$$

$$R_{BR}=a\left(\frac{1}{3600M_c}\frac{K_{CO}K_{f,B}\left(P_{CO}-\frac{P_{CO_2}}{P_{CO}K_{p,B}}\right)}{\left(1+K_{CO}P_{CO}+\frac{P_{CO_2}}{P_{CO}K_{CO}P_{CO}}\right)^2}\right) \quad (18)$$

Above-mentioned correlations for the rate of four dominant chemical reactions were used to calculate the sink or source terms for each gaseous specious inside the cell.

3. Mass Transfer Equation

Considering the multicomponent fluid flow and porous structure of the electrode, three mass transfer mechanisms, viscous flow, bulk diffusion and diffusion into the porous medium, are involved. As mentioned earlier, a syngas consisting of methane, hydrogen, carbon monoxide, carbon dioxide and water vapor is supplied to the fuel channel. On the other side a binary mixture of oxygen and nitrogen enters the air channel.

The unsteady state species mass conservation equations have been stated as follows:

$$\rho\frac{\partial\omega_i}{\partial t}+\nabla\cdot j_i+\rho(u\cdot\nabla)\omega_i=R_i \quad (19)$$

In this equation, parameters u, ω_i, j_i, and R_i stand for velocity field, mass fractions and source term. The relation between current density, mass fraction of each species and moles of transferred electrons can be written as follows [27];

$$N_i=j_i+\rho u\omega_i \quad (20)$$

$$j_i=-\rho\omega_i\sum D_{ik}d_k+D_i^T\frac{\nabla T}{T} \quad (21)$$

$$d_k=\nabla x_k+\frac{1}{P_A}[(x_k-W_k)\nabla P_A] \quad (22)$$

$$x_k=\frac{\omega_k}{M_k}M_n,\qquad M_n=\left(\sum\frac{\omega_i}{M_i}\right)^{-1} \quad (23)$$

The bulk diffusion coefficient can be calculated by use of the Fuller equation and a multi-component approach:

$$D_{b,i}=\frac{1-X_i^{fc}}{\sum_{j\neq i}\frac{X_i^{fc}\cdot\frac{P^{fc}}{10^5}\left[\frac{2}{M_i^{-1}+M_i^{-1}}\right]^{0.5}\cdot[V_{dif,i}^{1/3}+V_{dif,j}^{1/3}]^2}{1.43\times10^{-7}T_{fc}^{1.75}}} \quad (24)$$

With following definition for i and j:

i	j			
H_2	H_2O	CH_4	CO	CO_2
H_2O	H_2	CH_4	CO	CO_2
CO	H_2O	H_2	CH_4	CO_2
CO_2	H_2O	H_2	CH_4	CO

4. Heat Transfer

Unsteady state heat transfer equation in a porous matrix was used to determine the temperature distribution in the fuel cell:

$$(\rho C_p)^{eff}\frac{\partial T}{\partial t}+\rho C_p u\cdot\nabla\cdot T+\nabla\cdot q=Q \quad (25)$$

$$q=-K^{eff}\nabla\cdot T \quad (26)$$

k^{eff} and c_p^{eff} are the effective thermal conductivity and specific heat at constant pressure in porous electrode which can be calculated using the following correlations [29]:

$$K^{eff}=\varepsilon K_{gas}+(1-\varepsilon)K_{solid} \quad (27)$$

$$C_p^{eff}=\varepsilon C_{p,gas}+(1-\varepsilon)C_{solid} \quad (28)$$

Convective heat transfer between solid structures and fuel or air flows, conductive heat transfer in solid structures, considered endothermic and exothermic chemical reactions alongside electrochemical reactions, are the dominant heat transfer mechanisms and sink or source terms that are taken into account in the current model.

5. Carbon Deposition Model

Boudouard and methane cracking reactions occur within the anode diffusion and reaction layers [27]. The rate of carbon deposition inside the porous structures can be calculated as follows [27]:

$$r_c=\frac{dC_c}{dt}=a(R_{MCR}+R_{BR}) \quad (29)$$

Carbon gradually covers surfaces and reduces catalyst activity:

$$\frac{d\alpha}{dt}=-K_a r_c^2 C_c\alpha \quad (30)$$

Furthermore, carbon deposition reduces the porosity coefficient:

$$\frac{d\varepsilon}{dt}=\frac{dV_c}{dt}\frac{1}{V_{tot}}=\frac{\varepsilon r_c M_c}{\rho_c} \quad (31)$$

The variation of anode porosity would influence the permeability in porous layers:

$$K=K_0\left(\frac{\varepsilon}{\varepsilon_0}\right)^{3.55} \quad (32)$$

Local velocity, temperature, mole fraction, pressure, local chemical and electrochemical reactions affect the carbon deposition rate.

6. Boundary Conditions

Considering the mathematical nature of each unsteady conservation equation, initial values and proper boundary conditions must be considered. The cell operating voltage is implemented at the lower boundary of the anode support layer and the interface of electrode reaction layers, and electrolyte is assumed to be continuous. Velocity inlet boundary condition was chosen at the entrance of flow chan-

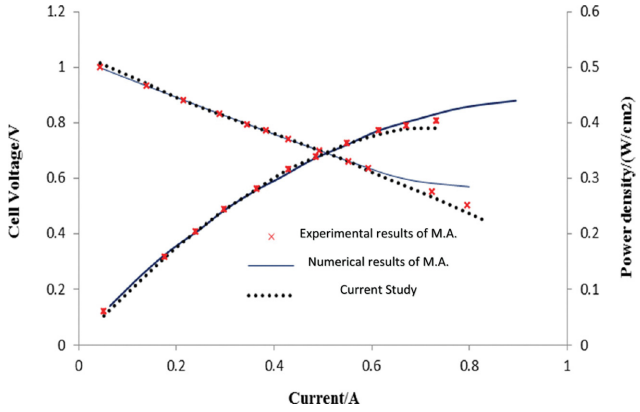

Fig. 3. Comparison between the measured and predicted performance.

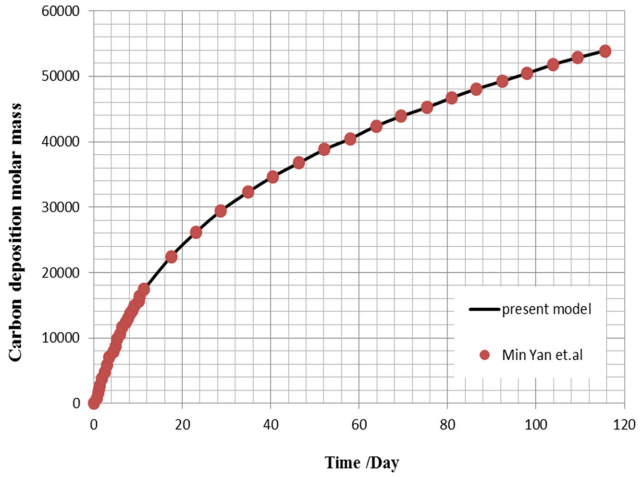

Fig. 4. Validation of carbon deposition.

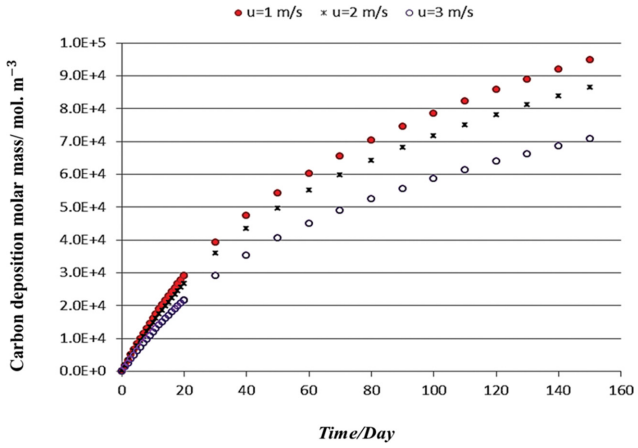

Fig. 5. Variation in carbon deposition in 150 days at variable velocity.

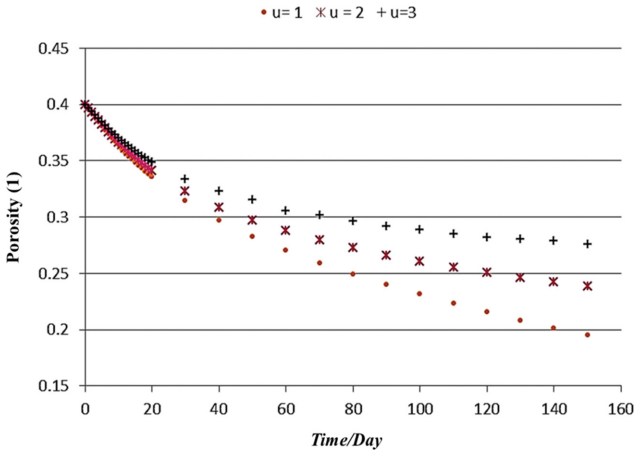

Fig. 6. Porosity variation in 150 days at variable velocity.

nels, while pressure outlet was specified at the outlet. For the species mass conservation equation, the mole fractions of each of gaseous species are assigned. To solve the energy conservation equation, the inlet temperature was implemented.

VALIDATION AND RESULT

To verify the results of the present study, an experimental report and two numerical solutions weren used. The comparison of the current model with the experimental data and numerical results of Anderson et al. [24] regarding the current density, cell voltage and power density are illustrated in Fig. 3. As can be seen, results are in sufficiently reasonable agreement with the literature. Furthermore, the results of Min Yan et al. [27] were used to validate the model performance in carbon deposition simulation. As can be seen from Fig. 4, the proposed model fully responded to the desired conditions with high accuracy.

1. Effect of Inlet Velocity on Carbon Deposition

The velocity of inlet gases is one of the effective parameters in the performance of the solid oxide fuel cell. Uniform input velocity is a boundary condition for the momentum and energy equations in the fuel channel. Three speeds of 1, 2, and 3 m/s were investigated to examine the effect of inlet velocity on the carbon deposition rates, and the results are shown in Figs. 5 and 6.

Changing the inlet velocity affects the rate of heat transfer in the cell and plays an important role in controlling the cell operating temperature and also reaction rate, such as methane cracking reaction. Less methane is consumed at high speeds or in other words, more methane is exhausted from the fuel cell without a reaction so there is less carbon deposited: as a result, less porosity change.

2. Effects of Inlet H_2 Molar Fraction on Carbon Deposition

The effect of variations in the molar fraction of the input hydrogen at 1,073 K and a velocity of 2 m/s on the rate of carbon deposition and variations in the porosity coefficient are illustrated in Figs. 7 and 8. The molar fraction ratio of H_2O/CH_4 is kept at 1, but the molar fraction of H_2O was changed. Increasing the inlet hydrogen ratio increases the electrochemical reaction rate. The higher current density creates a more significant average temperature and MCR rate; therefore, the carbon deposition rate increases, and the porosity coefficient decreases. However, increasing the amount of hydrogen increases the electric power.

3. Effect of Temperature on Carbon Deposition

As an important design and working parameter, fuel cell work-

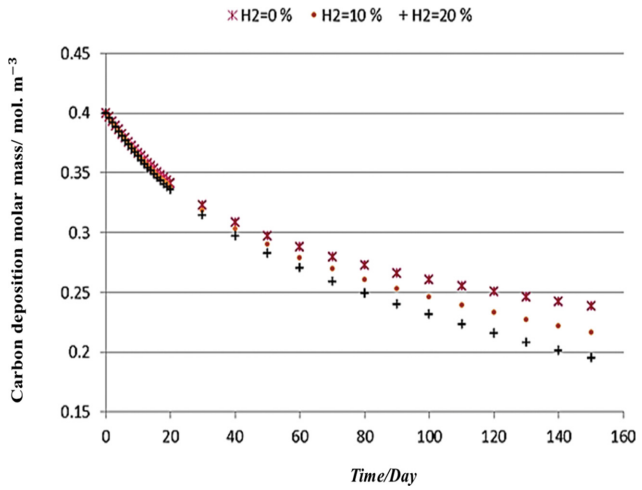

Fig. 7. Effect of inlet H_2 on porosity variation in 150 days.

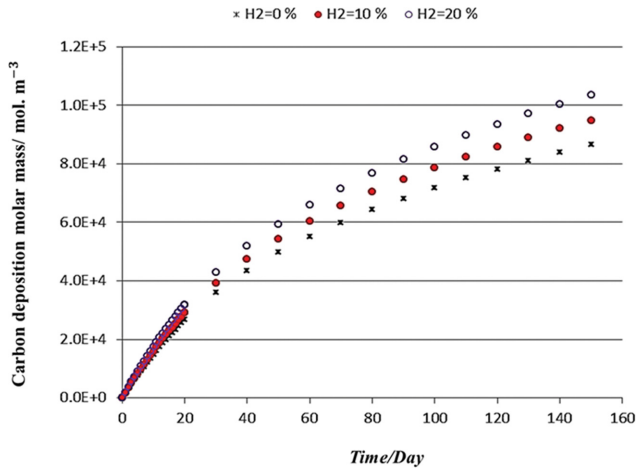

Fig. 8. Effect of inlet H_2 on carbon deposition in 150 days.

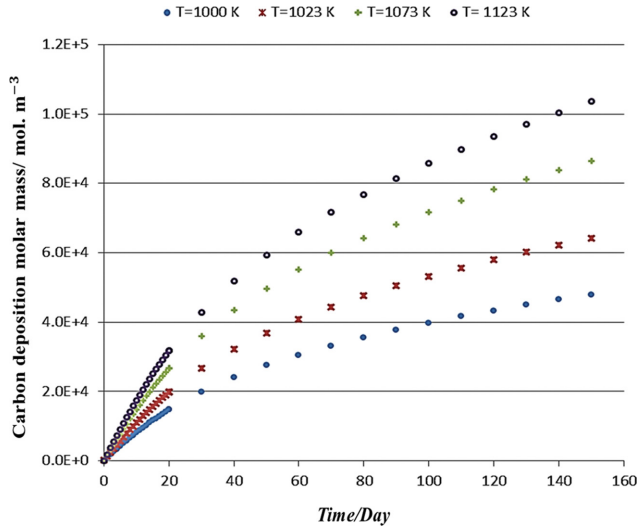

Fig. 9. Variation in carbon deposition in 150 days at variable temperatures.

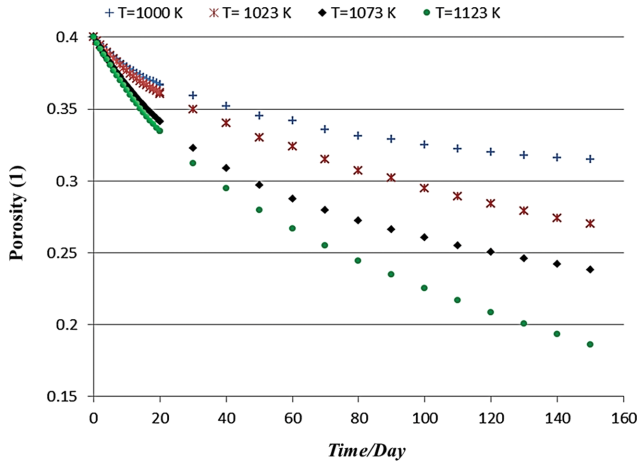

Fig. 10. Variation in porosity in 150 days at variable temperatures.

ing temperature, both in terms of efficiency and degradation resistance, is of great importance. In this section, the effects of temperature on carbon deposition and fuel cell efficiency are investigated. As it is shown in Fig. 4, the carbon deposition rate in the model increases by 33, 80, and 118% with increasing of the operating temperature from 1,000 to 1,023, 1,073, and 1,123 K, respectively, over a period of 150 working days. The higher the operating temperature, the higher the carbon deposition rate and the faster degradation of porous media. This phenomenon will lead to reduction in catalyst activity and ultimately the electric efficiency of the SOFC as depicted by Figs. 9 and 10.

4. Variations in Temperature Distribution Due to Carbon Deposition

Thermal stress and mechanical failure caused by local temperature hotspots are essential factors in a fuel cell, which occur due to the uneven temperature distribution between the cell and the reformer because of the mismatch between the endothermic reforming reactions and the exothermic reactions [33].

For this reason, the effect of carbon deposition at three inlet temperatures of 1,000 K, 1,023 K, and 1,073 K on the temperature distribution was investigated with considering endothermic reactions like MSRR and exothermic reactions like WGSR, BR, and electrochemical reactions. Results show that if there is no carbon deposition, the temperature distribution is assumed to be t=0, and the temperature along the fuel cell increases due to heat generation. However, with the deposition of carbon at 60 working days and 145 working days, the reaction rate gradually decreases, and the temperature variations along the fuel cell decrease. As can be seen, exothermic reactions are dominant reactions and temperature increase, but after 145 days since the heat generated by electrical current and electrochemical reactions has been greatly reduced, the MSR reaction, which is endothermic, the reaction prevails, so the temperature decreases first, but after consuming methane along the fuel cell, the heat reactions prevail and the temperature increases. As shown in Fig. 11(a)-(c), at the operating temperature of 1,000 K, the maximum output temperature reaches 1,050 K (the temperature at the end of the fuel cell and on the electrolyte). The output temperature decreases by 2.1% and 3.8% after 60 and 145 work-

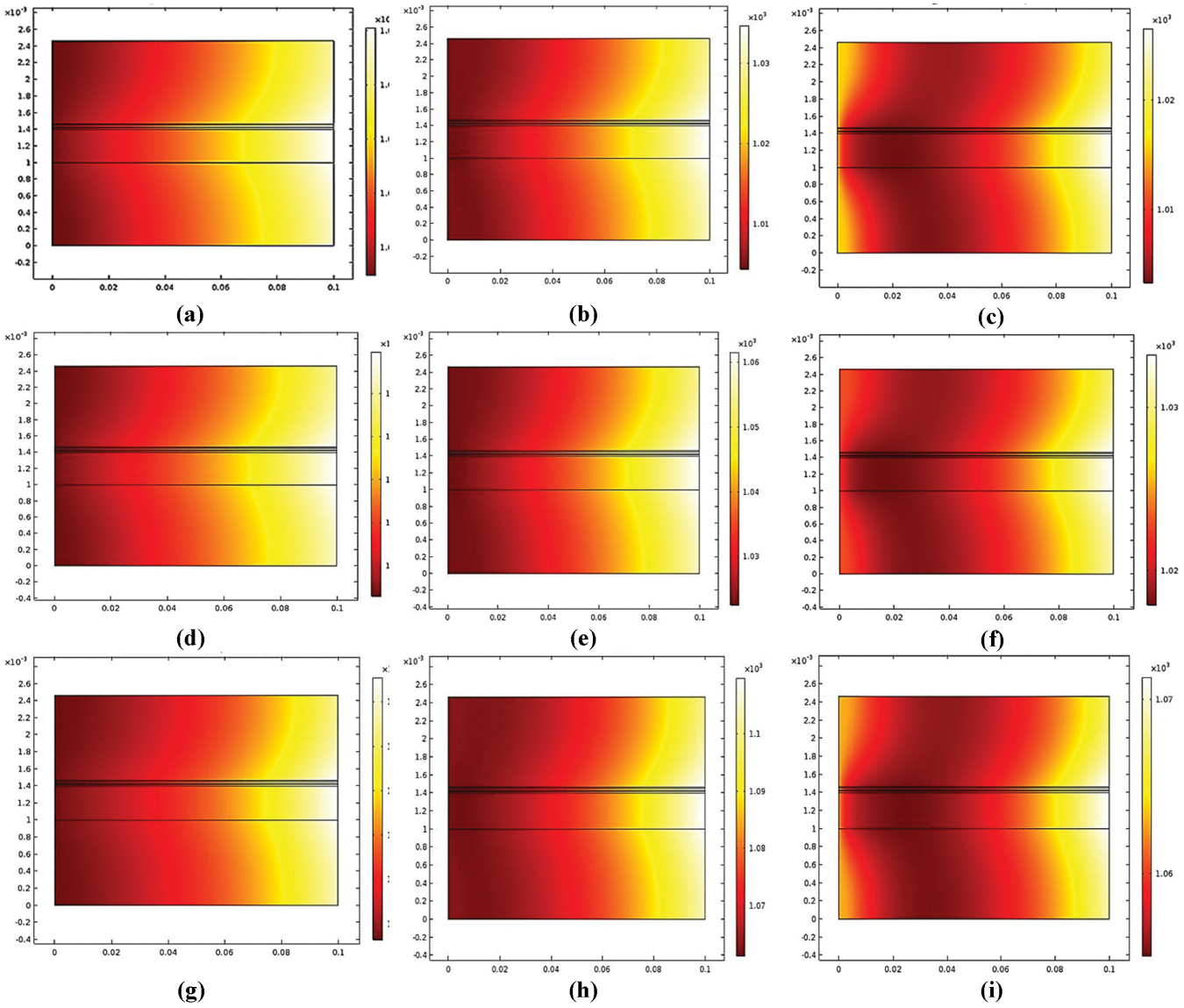

Fig. 11. Change in temperature distribution at different times and different operating temperatures. (a) at 1,000 K and t=0. (b) at 1,000 K and t=60. (c) at 1,000 K and t=145. (d) at 1,023 K and t=0. (e) at 1,023 K and t=60. (f) at 1,023 K and t=145. (g) at 1,073 K and t=0. (h) at 1,073 K and t=60. (i) at 1,073 K and t=145.

ing days, respectively; compared to the initial state of 1,050 K. Fig. 11(d)-(f) shows that the temperature distribution variations due to carbon deposition at the operating temperature of 1,023 K are much more significant. The maximum temperature of 1,080 K reaches 1,053 K and 1,034 K after 60 and 145 working days, respectively, i.e., a decrease of about 2.5 and 4.2 percent. As can be predicted and previously shown, by increasing the operating temperature to 1,073 K, the amount of carbon deposition and its effects increase, so the temperature variations increase. The temperature rate decreases in this case after working days of 60 and 145 by 5.8 and 9.2 percent.

5. Variation of Cell Performance at Different Temperatures

Carbon deposition has a significant effect on fuel cell performance. Fig. 12 shows the variations in fuel cell reactivity due to carbon deposition at different operating temperatures.

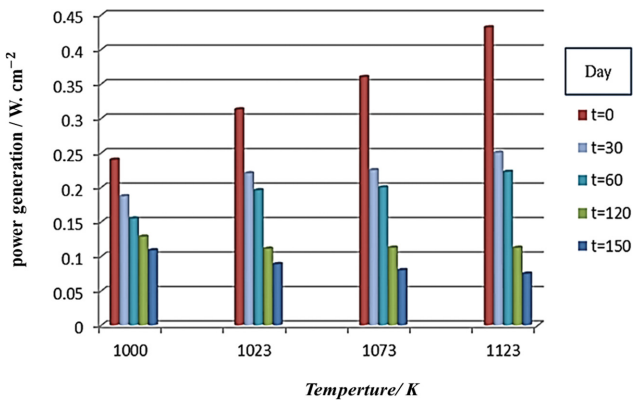

Fig. 12. Variation in fuel cell power generation due to carbon deposition at different temperatures and times.

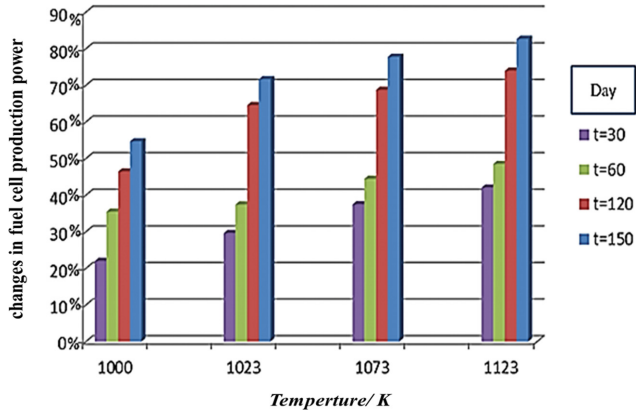

Fig. 13. Percentage of variation in fuel cell production power due to carbon deposition at different temperatures and times.

As is evident, the rate of electrochemical reactions varies significantly with increasing of the carbon deposition at higher temperatures with reducing of the porosity and catalyst activity. Fig. 13 shows variations in operating temperature over time to identify and compare these variations. At 1,123 K, after 150 working days, the generated power shows a decrease of 81%, which varies by 30% compared to 60 working days. The operating temperature of 1,000 K has the lowest percentage of variations with 52% over 150 working days. As observed from Figs. 12 and 13, at higher operating temperatures, the produced electric power is much higher, but the effect of carbon deposition is more significant.

CONCLUSION

The effect of carbon deposition on the electric performance of a methane fueled direct internal reforming planar SOFC was numerically investigated in two dimensions through COMSOL Multiphysics commercial software. Time dependent variation of porosity and catalyst activity affected by deposited carbon was modeled and verified against available experimental and numerical studies. Using proposed model the effect of SOFC some important operating parameters, such as fuel inlet velocity, the hydrogen mole fraction as one of the components of the entering fuel, and air and fuel inlet temperature on the rate of carbon deposition have been analyzed. It has been revealed that, any increase in inlet velocity of the fuel and decrease in entering hydrogen mole fraction will lead to decreased carbon deposition and thereby decreased porosity degradation which enhances the electric performance of the cell. On the other hand, it has been shown that increased fuel inlet temperature is the favorite of carbon deposition and deteriorates the cell output electric power and efficiency. Finally, it has been concluded that increasing the deposited carbon leads to decreased temperature gradient along the cell length, which results from reduced active area and chemical and electrochemical reaction rates.

NOMENCLATURE

C_C : molar concentration of carbon [mol m^{-3}]
C_{pi} : specific heat of species i at constant pressure [J mol^{-1} K^{-1}]
D_{ij} : binary diffusion coefficient [m^2 s^{-1}]
$\mathbf{E^0}$: Reversible electrical potential of cells at standard pressure and temperature [V]
$\mathbf{E^{REV}}$: reversible electrical potential of cells [V]
$\mathbf{E^{rev}_{H_2-O_2}}$: reversible electrical potential of cells, related to electrochemical reaction H_2 [V]
$\mathbf{E^{rev}_{CO-O_2}}$: reversible electrical potential of cells, related to electrochemical reaction CO [V]
$\mathbf{E_{cell}}$: electrical potential of cells [V]
F : Faraday's constant [C mol^{-1}]
J : current density [A m^{-2}]
k : thermal conductivity [W m^{-1} K^{-1}]
k_i : thermal conductivity of pure component I [W m^{-1} K^{-1}]
M : molecular weight of species I [kg mol^{-1}]
m_i : mass of species i [kg]
N_i : moles of electrons transferred per mole reactant [Mol m^{-2} s^{-1}]
n : moles of electrons transferred per mole reactant [mol]
n_i : moles of species i [mol]
p : pressure [Pa]
p_i : partial pressure of species i [Pa]
$\mathbf{P_i^{fc}}$: pressure of gas component in fuel channel [Pa]
$\mathbf{P_i^{fac}}$: pressure of gas component in the air channel [Pa]
$P^{ac}_{O_2}$: pressure of gas component in the air channel [Pa]
R_g : universal gas constant [J mol^{-1} K^{-1}]
R_wgsr : water-gas shift reaction rate [mol m^{-3} s^{-1}]
R_mcr : methane cracked reaction rate [mol m^{-3} s^{-1}]
R_msrr : methane steam reforming reaction rate [mol m^{-3} s^{-1}]
R_B : Boudouard reaction rate [mol m^{-3} s^{-1}]
RC : carbon deposition rate [mol m^{-3} s^{-1}]
$\dot{r}_{elc,\,CO}$: electrochemical reaction rate of CO component [mol m^{-2}·s^{-1}]
$\dot{r}_{elec,\,H_2}$: electrochemical reaction rate of H_2 component [mol m^{-2}·s^{-1}]
$\mathbf{\dot{r}_{elec,\,O_2}}$: electrochemical reaction rate of O_2 component [mol m^{-2}·s^{-1}]
S_i : source term of component i
T : temperature [K]
t : time [s]
u : velocity vector [m s^{-1}]
V_i : volume of species i [m^3]
w_i : mass fraction of species i
x_i : molar fraction of species i

Greek Symbols

ε : porosity [V]
ρ_i : density of species i [mol s^{-1}]

Subscripts

act : activity
an : anode
B : Boudouard reaction
Ca : cathode
cell : fuel cell
pore : porous media
R : methane steam reforming reaction
re : electrode reaction layer

S : CO water-gas shift reaction
st : electrode support layer
TPB : interface between anode and electrolyte

Superscripts
eff : effective

REFERENCES

1. M. Andersson, J. Yuan and B. Sundén, *Line approach and simulation for anode-supported SOFC*, ASME seventh international fuel cell science, Engineering and Technology Conference, June 8-10, Newport Beach, California, USA (2009).
2. M. Ni, *Int. J. Hydrogen Energy*, **37**(2), 1731 (2012).
3. P. W. Li, S. P. Chen and M. K. Chyu, *J. Fuel Cell Sci. Technol.*, **3**(2), 188 (2006).
4. Y. Patcharavorachot, A. Arpornwich-anop and A. Chuachuebsuk, *J. Power Sources*, **177**(2), 254 (2008).
5. I. Khazaee and A. Rava, *Energy*, **119**, 235 (2017).
6. Z. Xu, X. Zhang, G. Li, G. Xiao and J. Q. Wang, *Int. J. Hydrogen Energy*, **42**(16), 10785 (2017).
7. H. Xu and Z. Dang, *Int. J. Heat Mass Transfer*, **109**, 1252 (2017).
8. M. Borji, K. Atashkari, S. Ghorbani and N. Nariman-Zadeh, *J. Mech. Eng. Sci.*, **231**(4), 672 (2015).
9. M. C. Williams, J. P. Strakey, W. A. Surdoval and L. C. Wilson, *Solid State Ionics*, **177**(19), 2039 (2006).
10. S. McIntosh and R. J. Gorte, *Chem. Rev.*, **104**(10), 4845 (2004).
11. T. Ma, M. Yan, M. Zeng, J. l. Yuan, Q. Chen, B. Sundén and Q. W. Wang, *Appl. Energy*, **152**, 217 (2015).
12. S. Assabumrungrata, N. Laosiripojanab, V. Pavarajarna, W. Sangtongkitcharoen, A. Tangjitmateea and P. Praserthdama, *J. Power Sources*, **139**(1-2), 55 (2005).
13. T. Kim, G. Liu, M. Boaro, S. I. Lee, J. M. Vohs, R. J. Gorte, O. H. Al. Madhib and B. O. Dabbousi, *J. Power Sources*, **155**(2), 231 (2006).
14. C. Schluckner, V. Subotic, V. Lawlor and C. Hochenauer, *J. Fuel Cell Sci. Technol.*, **12**(5), 1053 (2015).
15. V. Subotic, C. Schluckner and C. Hochenauer, *J. Energy Inst.*, **89**(1), 121 (2016).
16. T. Kim, G. Liu, M. Boaro, S. I. Lee, J. M. Vohs, R. J. Gorte, O. H. Al. Madhib and B. O. Dabbousi, *J. Power Sources*, **155**(2), 231 (2006).
17. Y. Yang, X. Du, L. Yang, Y. Huang and H. Xian, *Appl. Therm. Eng.*, **29**(5-6), 1106 (2009).
18. H. Xu and Z. Dang, *J. Appl. Energy*, **178**, 294 (2016).
19. H. P. He and J. M. Hill, *Appl. Catal. A*, **317**(2), 284 (2007).
20. T. Chen, W. G. Wang, H. Miao, T. Li and C. Xu, *J. Power Sources*, **196**(5), 2461 (2011).
21. V. Alzate-Restrepo and J. M. Hill, *Appl. Catal. A*, **342**(1-2), 49 (2008).
22. J. H. Koh, Y. S. Yoo, J. W. Park and H. C. Lim, *Solid State Ionics*, **149**(3-4), 157 (2002).
23. C. Schluckner, V. Subotic, V. Lawlor and C. Hochenauer, *J. Fuel Cell Sci. Technol.*, **12**(5), 1053 (2015).
24. M. Andersson, J. Yuan and B. Sundén, *Appl. Energy*, **87**(5), 1461 (2010).
25. M. Borji, K. Atashkari, N. Nariman-zadeh and M. Masoumpour, *J. Mech. Eng. Sci.*, **229**(17), 3125 (2015).
26. V. M. Janardhanan and O. Deutschmann, *J. Power Sources*, **162**(2), 1192 (2006).
27. M. Yan, M. Zeng, Q. Chen and Q. Wang, *Appl. Energy*, **97**, 754 (2012).
28. Z. Jaworski and P. Pianko-Oprych, *Int. J. Hydrogen Energy*, **42**(27), 16920 (2017).
29. M. M. Hussain, X. Li and I. Dincer, *J. Power Sources*, **189**(2), 916 (2009).
30. P. Costamagna and K. Honegger, *J. Electrochem. Soc.*, **145**(11), 3995 (1998).
31. O. Razbani, M. Assadi and M. Andersson, *Int. J. Hydrogen Energy*, **38**(24), 10068 (2013).
32. P. Sarmah, T. K. Gogoi and R. Das, *Appl. Therm. Eng.*, **119**, 98 (2017).
33. P. Dokmaingam, J. T. S. Irvine, S. Assabumrungrat, S. Charojrochkul and N. Laosiripojana, *Int. J. Hydrogen Energy*, **35**(24), 13271 (2010).
34. H. Iwai, Y. Yamamoto, M. Saito and H. Yoshida, *J. Energy*, **36**(4), 2225 (2011).